Supramolecular ferroelectric nematic materials

Richard J. Mandle

Published online: 14 Nov 2022.

Submit your article to this journal ⬚

Article views: 422

View related articles ⬚

View Crossmark data ⬚

Supramolecular ferroelectric nematic materials

Richard J. Mandle 🆔 [a,b]

[a]School of Physics and Astronomy, University of Leeds, Leeds, UK; [b]School of Chemistry, University of Leeds, Leeds, UK

ABSTRACT
The discovery of a new nematic phase variant with polar order and ferroelectricity, the N_F phase, is a significant milestone in soft matter research. Herein we describe the preparation of hydrogen-bonded complexes between 4-(2,4-dimethoxybenzoyloxy)benzoic acid and either 4-nitropyridine or 3-fluoro-4-nitropyridine, these being analogous in structure to the archetypal N_F material *RM734*. Complexes were isolated using a semi-automated process we term Machine Vision Aided Crystallisation. We find these complexes exhibit classical and polar (N_F) nematic phases despite the large reduction in electric dipole moment that results from swapping a phenyl ring for 4-pyridyl. DFT calculations support the hypothesis that the onset of polar order is not simply a product of electric dipole magnitude, but rather results from more subtle interactions between regions of opposing electrostatic potential.
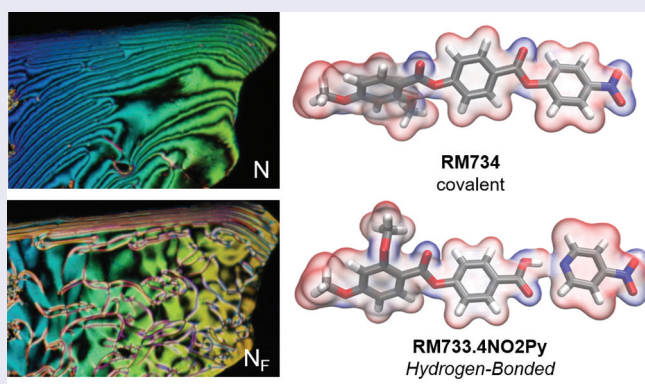
Introduction

Nematic liquid crystals are ubiquitous in our daily lives thanks to their use in display technology [1]. The constituent molecules of the nematic phase have – on average – a preferred direction of orientation termed the director. The nematic liquid crystals we encounter day-to-day are *apolar*; despite their bulk orientational order, with the molecules showing having an equal probability of being orientated parallel or antiparallel to the director (Figure 1(a)). Nematic and smectic phases with polar order (Figure 1(b)) have recently been realised experimentally [2–6], presenting an interesting counterpoint to the apolar nematics we encounter daily. Notably, two materials were reported in 2017 – *RM734* (Figure 1(c)) [7] and *DIO* [8] – that are now understood to have polar nematic order and are ferroelectric [2–4]. This so-called ferroelectric nematic (N_F) phase displays properties distinct from

those of the conventional *apolar* nematic: ferroelectricity, with large spontaneous polarisation [3,9]; polar domains [9]; strong non-linear optical response [10]; unique electrooptic responses [11]; thermal gradient-induced circular motion of particles [12]. Progress in understanding and exploiting the unique physics of the N_F phase is reliant on the design and synthesis of new materials, with significant progress since the report of the first polar nematic materials in 2017 [7,8,13–21]. The N_F materials reported to date are exclusively rod-like, with polar groups (for example nitro, fluoro, cyano, esters, difluoromethoxy) oriented such that there is a large molecular electric dipole moment which is oriented close to parallel to the molecules long axis. Around 200 compounds have been reported in the literature as exhibiting the N_F [7,13–23], and these are presently restricted to covalently bonded materials. With hydrogen-bonded supramolecular
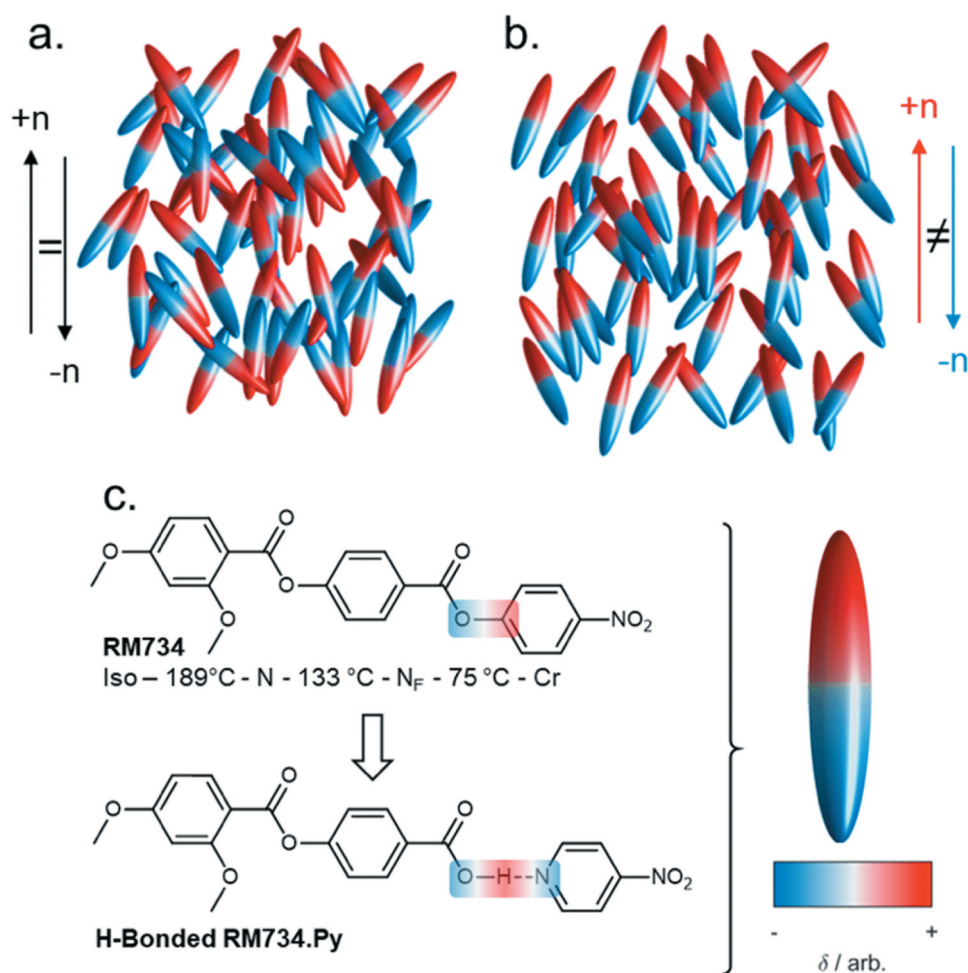
Figure 1. (Colour Online) Programmatically generated cartoon depictions of ellipsoids forming a conventional apolar nematic phase (a) and polar nematic phase (b), with order parameters (<P2>) of 0.60 and 0.67, respectively. (c) Molecular structure and transition temperatures of RM734 and a homologous hydrogen-bonded complex synthesised as part of this work. An idealised polar ellipsoid representation of molecular structure is used elsewhere in this figure, with the red/white/blue colouring used to illustrate regions of electronegativity/electropositivity.

liquid crystals being well established [24], we consider that, *a priori*, supramolecular systems should be capable of generating polar nematic phases. Furthermore, the large charges that can be associated with (for example) hydrogen-bonded systems might even confer advantageous increases in dipole moment.

Methods

Experimental

The N_F material RM734 was synthesised according to the original report by Mandle *et al.* [7]. The precursor carboxylic acid, 4-nitropyridine [25] and 3-fluoro-4-nitropyridine [26] were synthesised according to precedent. Repeated attempts to form the target hydrogen-bonded complexes (Figure 2(a)) using commercially sourced 4-nitropyridines were met with failure; we

attribute this to varying (and typically high) degrees of autoxidation to the N-oxide derivative. Synthesised 4-nitropyridines were stored under nitrogen at −20°C and were used within 6 h of synthesis. The hydrogen-bonded complexes were prepared as shown in scheme 1: the carboxylic acid (1 mmol) was suspended in acetone (3.5 ml) in a 7 ml vial, and vigorously stirred under an atmosphere of nitrogen gas. The suspension was partially dissolved by heating to 50°C, before adding a solution of the pyridine derivative (1 mmol) in acetone (0.5 ml), prompting a slight exotherm and affording a near homogenous solution. The solution was stirred for 1 h at 50°C before cooling to ambient temperature.

In exploratory experiments, we observed isolation of the resultant hydrogen bonded complexes to be rather problematic; we suspect that autoxidation of the uncomplexed nitropyridine to the n-oxide occurs rapidly; thus, the pyridine dosing is substoichiometric,
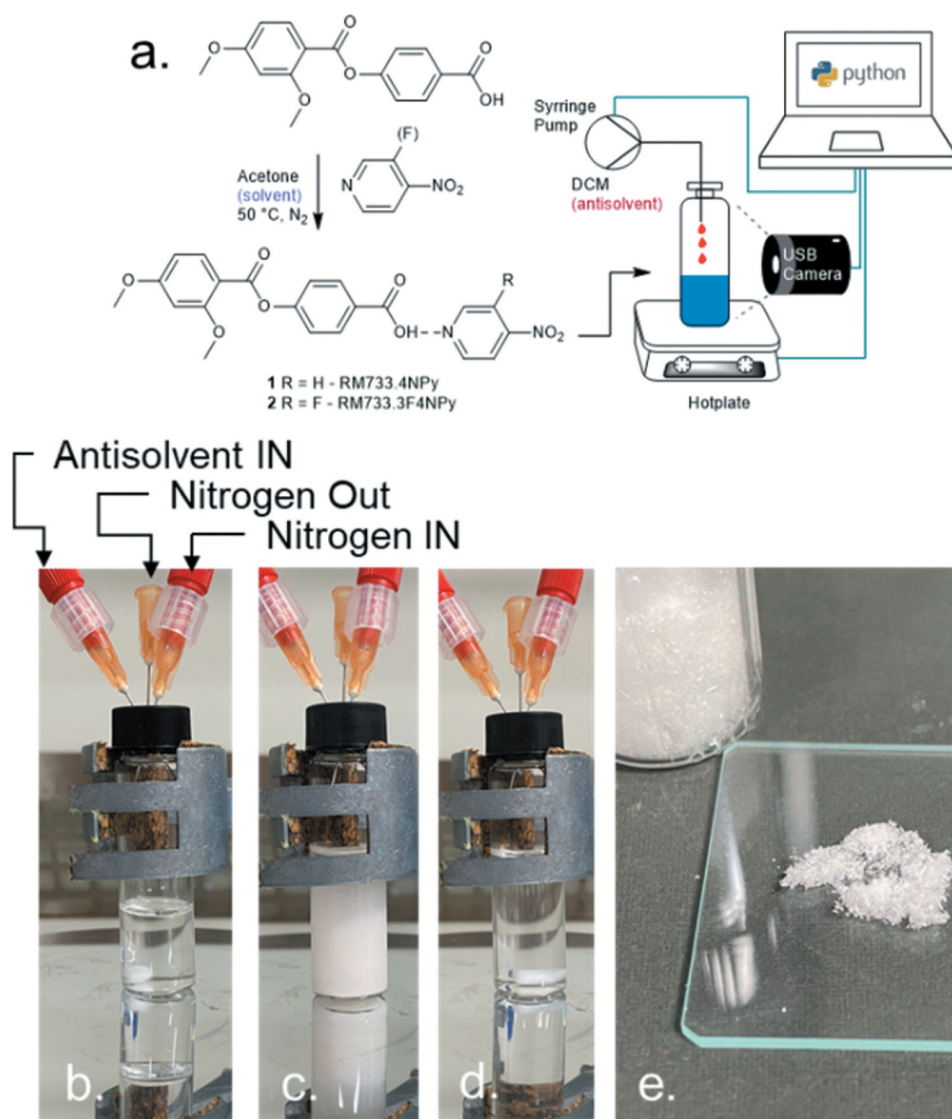
Figure 2. (Colour Online) (a) Synthetic scheme for the synthesis of complexes 1 (Rm733.4npy) and 2 (Rm733.3f4npy), including the MVAC process. Photographs captured during the MVAC process for **2**: (b) initial state (complex dissolved in acetone); (c) turbid state (maximum antisolvent concentration reached, complex precipitated); (d) final state (complex redisolved with heating); (e) complex **2** isolated as a colourless microcrystalline solid following suction filtration and drying.

leading to a mixture of acid, n-oxide and the desired complex. We, therefore, purify the resultant complexes from the reaction solution using Machine Vision Aided Crystallisation (MVAC). This process takes advantage of the near total insolubility of the precursor acid in acetone, the insolubility of the complexes in acetone/ DCM mixtures and the solubility of the pyridines and their N-oxides in both solvent systems. For MVAC, the reaction suspension is filtered through a 0.2 micron PTFE filter to remove any uncomplexed carboxylic acid, before transferring to a 7 ml vial and concentrating to a volume of 2 ml (Figure 2(b)). The vial containing the filtered solution of hydrogen-bonded complex is placed on a hotplate (IKA RCT Digital) at ambient temperature, and vigorously stirred. A PC-controlled syringe pump (New Era) delivers 100 µl of DCM (as an antisolvent) into the vial as a bolus every 300 s, with mixing ensured by stirring (500 rpm). Machine vision *via* a USB camera monitors the addition process; as antisolvent is added the solution becomes turbid due to precipitation, with homogeneity restored by mixing. When the turbidity/precipitation persists for more than 150 s, the antisolvent addition is discontinued; the vial is then allowed to stand for 1 h to allow total precipitation of the complex (Figure 2(c)). The PC then turns on the hotplate heater, warming the vial to 40°C, resulting in a homogenous solution (Figure 2(d)). At this point, heating and stirring are discontinued and the solution

left to stand for 24 h at ambient temperature, giving the target complexes as crystalline solids which we isolate and dry with filtration, with any uncomplexed nitropyridine or nitropyridine n-oxide remaining in solution (Figure 2(e)). The software that controls the MVAC process is written in Python; solvent volumes, turbidity and temperatures are logged, along with captured images, enabling reproduction or scale up.

Instrumentation

Polarised optical microscopy was performed on a Leica DMLP polarising microscope with temperature control *via* a Linkam TMS94 hotstage and controller. Photomicrographs were captured using a Nikon D7200 DLSR mounted atop the microscope. Differential scanning calorimetry employed a TA instruments DSC Q20 at a heat/cool rate of 10°C min^{-1}, operating under an atmosphere of dry nitrogen.

Mixture formulation

We prepared binary mixtures by combining precisely weighed quantities of hydrogen-bonded complex with RM734 and dissolving into the minimum volume of warm acetone, aided by ultrasonication. Homogeneity was ensured by ultrasonication (1 min) and then vortex mixing (1500 rpm, 1 min). The solvent was removed by heating, and the process repeated a total of three times to give homogenous samples.
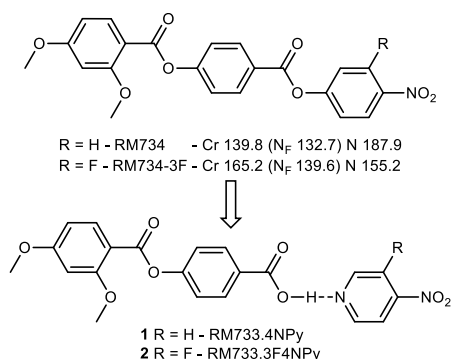
Computational

Electronic structure calculations were performed in Gaussian G09 rev d01 [27] with the B3LYP hybrid functional [28] and the 6-31 G(d,p) basis set with Grimme's GD3 dispersion correction with Becke-Johnson damping (GD3BJ) [29], and counterpoise correction for hydrogen-bonded complexes. The absence of imaginary frequencies in a subsequent frequency calculation confirms that the resultant structures are indeed an energy minimum. We generated electrostatic potential (ESP) isosurfaces (electron density maps from total SCF density mapped with ESP) for the complexes at the B3LYP-GD3BJ/6-31 G(d,p) level of DFT using Gaussian G09 rev d01.

Results

The mesomorphic behaviour of both complexes, determined by a combination of polarised optical microscopy (POM) and differential scanning calorimetry (DSC), is given in Table 1.

Both complexes display significant increases in melting point when compared to the parent materials (RM734, RM734-3F). Both the precursor acid and 4-nitropyridines are non-mesogenic; with the former having a melting point of 219°C and recrystalising at 200°C. Complexes **1** and **2** both melt directly into the isotropic liquid, and on cooling exhibits two distinct nematic phases. The upper temperature phase is a conventional nematic, whereas the lower temperature

Table 1. Transition temperatures (T, °C) and associated enthalpies (ΔH, kJ mol^{-1}) for the complexes **1** (Rm733.4npy) and **2** (Rm733.3f4npy). Transition temperatures for the analogous parent covalent materials *RM734* and *RM734-3F* are given, above. # Transition observed by POM only. * the complex begins to decompose at 250°C.

R = H - RM734   - Cr 139.8 (N$_F$ 132.7) N 187.9
R = F - RM734-3F - Cr 165.2 (N$_F$ 139.6) N 155.2

1 R = H - RM733.4NPy
2 R = F - RM733.3F4NPy

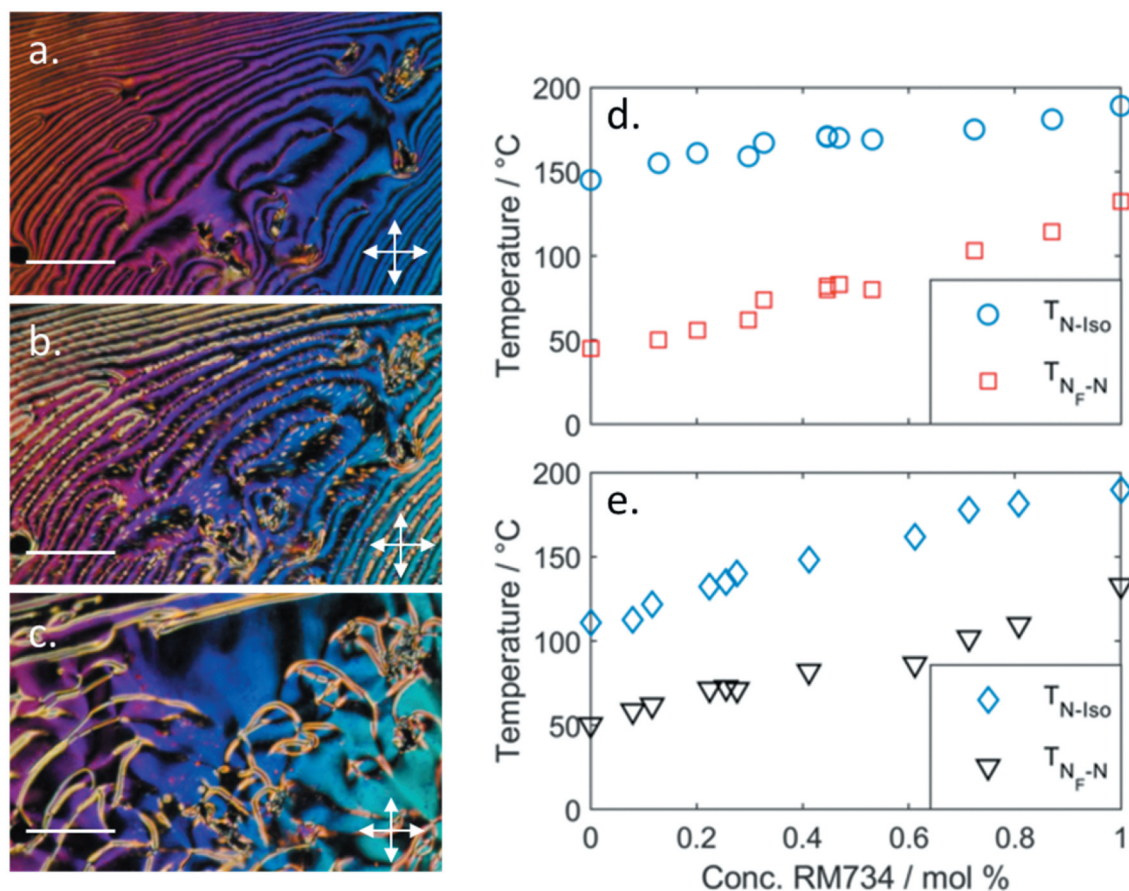| No.	R =		Melt	N$_F$-N	N-Iso
1	H	T	225	45$^\#$	145
RM733.4NPy		ΔH	50.6	-$^\#$	0.3
2	F	T	239*	50$^\#$	110.9
RM733.3F4NPy		ΔH	47.1	-$^\#$	0.6

Figure 3. (Colour Online) Photomicrographs of complex **1**: (a) the *schlieren* texture of nematic phase at 67°C; (b) at N_F-N transition at 45°C; (c) the *schlieren* texture of the N_F phase at 41°C. Photomicrographs a–c are of the same region of the sample, with the scale bar corresponding to 50 μm. Phase diagrams for binary mixtures of: (d) complex **1** and RM734; (e) complex **2** and RM734; note that melting points are omitted for clarity.

phase is a ferroelectric nematic (*vide infra*). The higher temperature (apolar) nematic phase displays a characteristic *schlieren* texture (Figure 3(a)), which becomes grainy at the N_F-N transition (Figure 3(b)), while the lower temperature (polar/ferroelectric) nematic phase displays a *schlieren* texture with a modest change in birefringence (Figure 3(c)). Microscopy studies of complexes **1** and **2** are consistent with those on other N_F materials [8,21]. Complex **1** has a wider nematic phase range than the fluorinated

complex **2**, mirroring the behaviour of the parent systems. The fact that hydrogen-bonded systems can display the N_F phase is encouraging; nevertheless, it must be acknowledged that, in the present case, the onset temperature of the N_F phase is far below the melting point, which renders detailed characterisation of these complexes virtually impossible. We constructed a phase diagram for binary mixtures of each complex in turn with RM734 (Figure 1(c)) in order to validate our phase assignment of both phases. Both hydrogen-bonded

Table 2. Dipole moment (μ, Debye), dipole angle (β, °) and anisotropy of polarizability (Δα, Å^3) for complexes **1** and **2**, along with the parent covalent materials *RM734* and *RM734-3F*, as calculated at the B3LYP-GD3BJ/6-31 g(d,p) level. Shape Anisotropy Parameter (*ShAP*) defined here as $l/\sqrt{(wb)}$, where $l/w/b$ are the molecular length, width and breadth, respectively.

No.	μ	β	Δα	ShAP
1	5.7	22.1	39.4	5.39
2	6.6	24.5	39.4	5.13
RM734	11.4	15.5	47.5	4.07
RM734-3F	12.3	15.6	48.5	4.34

complexes are miscible with RM734 across the entire phase diagram, with the onset temperatures of the nematic and N_F phases varying approximately linearly with concentration (Figure 3(d,e)), confirming the earlier phase assignment made by microscopy.

We performed geometry optimisations for both complexes at the B3LYP-GD3BJ/6-31 G(d,p) level of DFT, as well as for the analogous covalently bonded materials (*RM734* and *RM734-3F*). For the hydrogen-bonded systems, we also employ counterpoise correction in our DFT methods; the complexation energies are 56 kJ mol^{-1} and 53 kJ mol^{-1} for **1** and **2**, respectively. Our calculations show that complexes **1** and **2** have smaller dipole moments than the parent systems (Table 2). The angle between the dipole vector and the long axis (β) is also being somewhat larger for the complexes than the covalently bonded systems. As expected, the anisotropy of polarisability in **1** and **2** is reduced, relative to the parent compounds, owing to the fact that the aromatic core units are not covalently bonded. The increased

molecular length of complexes **1** and **2** relative to RM734/RM734-3F leads to marginally higher values of the shape anisotropy parameter (ShAP). While the molecular electric dipole moment does not govern the incidence of the N_F phase in isolation, the magnitude of the reduction in the hydrogen-bonded complexes, relative to the parent systems, is very much consistent with the reduction in $T_{N\text{-} N_F}$ seen for complex **1**. More surprising is that complex **1**, whose dipole moment is only around 25% larger than that of 5CB (4.5 D), being capable of sustaining the polar order that generates the N_F phase at all, albeit at a very significantly reduced onset temperature to the covalently bonded parent material.

Results for complexes **1/2** imply that the molecular electric dipole moment is not the sole genesis of polar order in nematics, and we, therefore, considered the role of more subtle electrostatic interactions. We first consider the molecular electrostatic potential on the 0.001 au electron density isosurface of *RM734* (Figure 4(a));
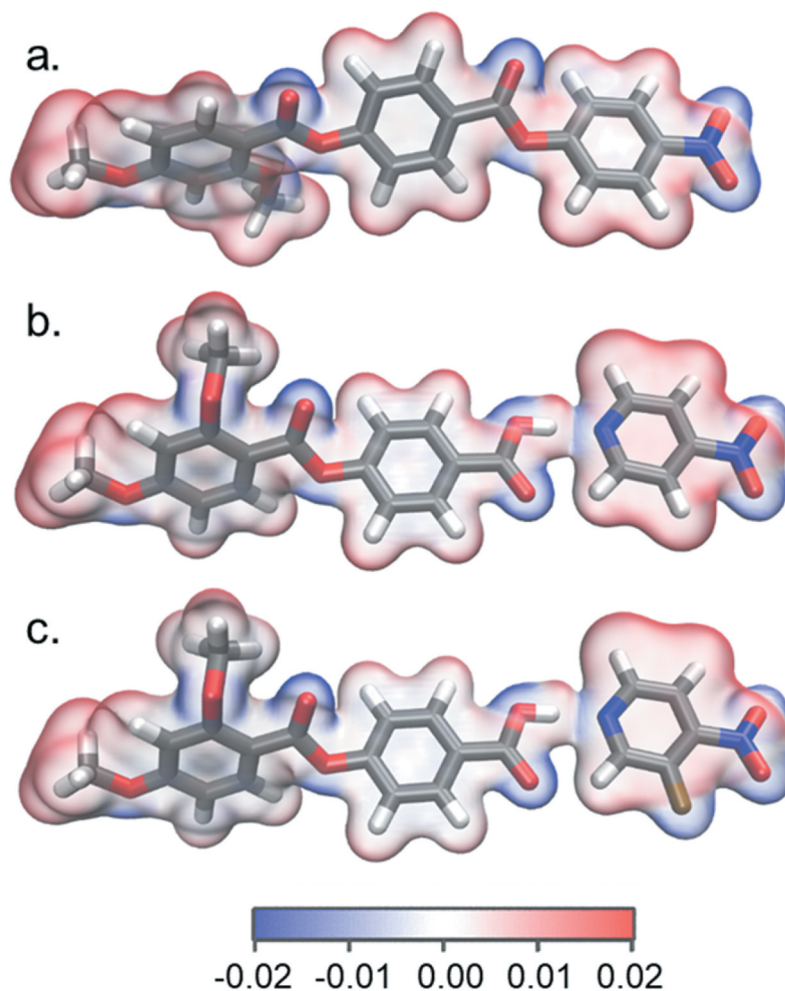

Figure 4. (Colour Online) Optimized geometries of RM734 (a) and complexes **1** (b) and **2** (c) at the B3LYP-GD3BJ/6-31g(d,p) level of DFT, with the electrostatic potential (ESP, isovalue = 0.04 au) on the 0.001 au electron density isosurface.

this shows alternating regions of electronegativity/electropositivity that result from the esters/nitro and alkyl/aryl units, respectively. In complexes **1** and **2,** these regions of opposite potential are retained, and augmented by large charges localised around the pyridinium-carboxylate portion. The importance of these alternating regions of positive and negative electrostatic potential is not entirely clear; however, it can be envisioned that the alternating ESP charges give rise to relatively strong electrostatic interactions between adjacent molecules. Simple inspection of the isosurface data reveals that the terminal CH_3 and NO_2 groups – both of which are found in RM734 and also **1/2** – have the largest electropositivity/negativity, respectively, presenting a clear route to polar head-to-tail pair formation. We consider that these strong electrostatic interactions most likely contribute to emergent polar order in conjunction with dipole–dipole interactions, by favouring (slightly) the formation of parallel over antiparallel pairs through some sort of biasing steric pressure.

In future, it might perhaps be desirable to utilise the electronegativity of the pyridine nitrogen atom to contribute towards the electric dipole moment of the molecule rather than working against it as it does here. We have synthesised the 4-nitro-3-pyridyl analogues of RM734 and related materials (most of which display enhanced N_F phase stability relative to the progenitor material) and investigation of their resulting complexes is one direction for future research. Equally, we do not expect supramolecular N_F materials to be restricted to the H-bond donor (carboxylic acid) and acceptor (pyridine) combination detailed here, and complexes formed by other strong non-covalent interactions such as halogen-bonding (e.g. pyridine + iodinemonochloride) also appear worthy of investigation.

Conclusions

Here, we present the first study on hydrogen-bonded complexes within the context of the ferroelectric nematic phase. The reported complexes are analogous in structure to RM734, with the terminal 4-nitrophenyl unit replaced with a 4-nitropyridyl. We developed a novel computer-controlled purification process that greatly simplifies the isolation of both complexes. Compared to the parent covalent materials, the hydrogen-bonded complexes have higher melting points and greatly diminished mesophase onset temperatures. We attribute this to the significantly reduced dipole moment that results from having a nitrogen atom *para* to the nitro group of the terminal ring. However, the fact that complex **1** forms an N_F phase at all is remarkable given that its dipole moment is only around 25% larger than

that of 5CB. DFT calculations reveal that both covalent materials (RM734, RM734-3F) and complexes **1** and **2** have alternating regions of positive and negative electrical charge, and we suggest that these have an important role in promoting polar order. Looking forward, hydrogen-bonded analogues of other N_F materials that lack terminal nitro groups (e.g. DIO) appear particularly attractive as a means to avoid the autoxidation associated with 4-nitropyridine and its derivatives, as do complexes formed by other strong non-covalent interactions (e.g. halogen bonds).

Disclosure statement

No potential conflict of interest was reported by the author.

ORCID

Richard J. Mandle ⓘD http://orcid.org/0000-0001-9816-9661

References

[1] Bremer M, Kirsch P, Klasen-Memmer M, et al. The TV in your pocket: development of liquid-crystal materials for the new millennium. Angewandte Chemie. 2013;52 (34):8880–8896.

[2] Mertelj A, Cmok L, Sebastian N, et al. Splay nematic phase. Phys Rev X. 2018;8(4). DOI:10.1103/PhysRevX.8.041025

[3] Chen X, Korblova E, Dong D, et al. First-principles experimental demonstration of ferroelectricity in a thermotropic nematic liquid crystal: polar domains and striking electro-optics. PNAS. 2020;117 (25):14021–14031.

[4] Mandle RJ, Sebastián N, Martinez-Perdiguero J, et al. On the molecular origins of the ferroelectric splay nematic phase. Nat Commun. 2021;12(1):4962.

[5] Kikuchi H, Matsukizono H, Iwamatsu K, et al. Fluid layered ferroelectrics with global C∞v symmetry. Adv Sci. 2022;9(26):2202048.

[6] Chen X, Martinez V, Nacke P, et al. Observation of a uniaxial ferroelectric smectic a phase. arXiv preprint arXiv:12965. 2022.

[7] Mandle RJ, Cowling SJ, Goodby JW. Rational design of rod-like liquid crystals exhibiting two nematic phases. Chem Eur J. 2017;23(58):14554–14562.

[8] Nishikawa H, Shiroshita K, Higuchi H, et al. A fluid liquid-crystal material with highly polar order. Adv Mater. 2017;29(43):1702354.

[9] Sebastian N, Cmok L, Mandle RJ, et al. Ferroelectric-ferroelastic phase transition in a nematic liquid crystal. Phys Rev Lett. 2020;124(3):037801.

[10] Folcia CL, Ortega J, Vidal R, et al. The ferroelectric nematic phase: an optimum liquid crystal candidate for nonlinear optics. Liq Cryst. 2022;49(6):899–906.

[11] Sebastian N, Mandle RJ, Petelin A, et al. Electrooptics of mm-scale polar domains in ferroelectric nematic phase. Liq Cryst. 2021;48(14):2055–2071. Internet. DOI:10.1080/02678292.2021.1955417.

[12] Tibor Máthé M, Buka Á, Jákli A, et al. Ferroelectric nematic liquid crystal thermo-motor. ArXiv e-prints. 2022;105(5):arXiv:2201.07556.

[13] Song Y, Li J, Xia R, et al. Development of emergent ferroelectric nematic liquid crystals with highly fluorinated and rigid mesogens. Phys Chem Chem Phys. 2022;24(19):11536–11543.

[14] Li J, Wang Z, Deng M, et al. General phase-structure relationship in polar rod-shaped liquid crystals: importance of shape anisotropy and dipolar strength. Giant. 2022;11:100109.

[15] Saha R, Nepal P, Feng C, et al. Multiple ferroelectric nematic phases of a highly polar liquid crystal compound. arXiv e-prints. 2021:arXiv:2104.06520.

[16] Mandle RJ, Cowling SJ, Goodby JW. Structural variants of RM734 in the design of splay nematic materials. Liq Cryst. 2021;48(12):1780–1790.

[17] Manabe A, Bremer M, Kraska M. Ferroelectric nematic phase at and below room temperature. Liq Cryst. 2021;48(8):1079–1086.

[18] Li J, Nishikawa H, Kougo J, et al. Development of ferroelectric nematic fluids with giant-ε dielectricity and nonlinear optical properties. Sci Adv. 2021;7(17): eabf5047.

[19] Dai S, Li J, Zhou J, et al. Polar liquid crystalline polymers bearing mesogenic side chains with large dipole moment. Macromolecules. 2021;54(13):6045–6051.

[20] Brown S, Cruickshank E, Storey JMD, et al. Multiple polar and non-polar nematic phases. Chem Phys Chem. 2021;22(24):2506–2510.

[21] Mandle RJ, Cowling SJ, Goodby JW. A nematic to nematic transformation exhibited by a rod-like liquid crystal. Phys Chem Chem Phys. 2017;19(18):11429–11435.

[22] Zhao X, Zhou J, Li J, et al. Spontaneous helielectric nematic liquid crystals: electric analog to helimagnets. PNAS. 2021;118(42):e2111101118.

[23] Pociecha D, Walker R, Cruickshank E, et al. Intrinsically chiral ferronematic liquid crystals: an inversion of the helical twist sense at the chiral nematic - chiral ferronematic phase transition. J Molec Liq. 2022;361:119532.

[24] Paleos CM, Tsiourvas D. Supramolecular hydrogen-bonded liquid crystals. Liq Cryst. 2001;28(8):1127–1161.

[25] Karramkam M, Hinnen F, Vaufrey F, et al. 2-, 3- and 4-[18f]fluoropyridine by no-carrier-added nucleophilic aromatic substitution with K[18F]F-K222 – a comparative study. J Labelled Compd Rad. 2003;46(10):979–992.

[26] Brugarolas P, Inventor; Pedro Brugarolas Synthesis of meta-substituted [18F]-3-fluoro-4-aminopyridines by direct radiofluorination of pyridine N-oxides, US Patent no US10160695B2, 2017.

[27] Frisch MJ, Trucks GW, Schlegel HB, et al. 09 rev d01. 2009

[28] Becke AD. Density-functional thermochemistry. III. The role of exact exchange. J Chem Phys. 1993;98 (7):5648–5652.

[29] Grimme S, Ehrlich S, Goerigk L. Effect of the damping function in dispersion corrected density functional theory. J Comput Chem. 2011;32(7):1456–1465.